

Antiferromagnetic ordering and strain effects in monolayer quadrilateral FeS_2

Zhihao Li(李志豪), Junlin Wang(王君林), Guanqi Li(李冠祺), Yao Li(黎遥), Liang He(何亮), Jing Wu, Yongbing Xu, Xianyang Lu(陆显扬)

Citation: Chin. Phys. B. 35, 098503 (2026). DOI: 10.1088/1674-1056/ae1c1f | CSTR: 32038.14.CPB.ae1c1f
http://cpb.iphy.ac.cn; http://iopscience.iop.org/cpb

What follows is a list of articles you may be interested in

Strain-mediated voltage control of skyrmion transport in nanoracetracks

Hao-Yuan Wang(王灏元), Xue-Feng Zhang(张雪枫), Tian Qiu(邱添), Huiting Li(李慧婷), Xiao-Ping Ma(马晓萍), Je-Ho Shim(沈帝虎), Xing-Ri Jin(金星日), Hong-Guang Piao(朴红光)
Chin. Phys. B. 35, 068502 (2026). DOI: 10.1088/1674-1056/ae3233 | CSTR: 32038.14.CPB.ae3233

Strong enhancement of spin–orbit torques and perpendicular magnetic anisotropy in $[Pt_{0.75}Ti_{0.25}/Co–Ni\ multilayer/Ta]_n$ superlattices

Xiaomiao Yin(阴小苗), Zhengxiao Li(李政霄), Jun Kang(康俊), Changmin Xiong(熊昌民), Lijun Zhu(朱礼军)
Chin. Phys. B. 35, 018502 (2026). DOI: 10.1088/1674-1056/ae1c26 | CSTR: 32038.14.CPB.ae1c26

Interlayer exchange coupling effects on the spin–orbit torque in synthetic magnets

Haodong Fan(樊浩东), Zhongshu Feng(冯重舒), Tingwei Chen(陈亭伟), Xiaofeng Han(韩晓峰), Xinyu Shu(舒新愉), Mingzhang Wei(卫鸣璋), Shiqi Liu(刘士琦), Mengxi Wang(王梦溪), Shengru Chen(陈盛如), Xuejian Tang(唐学健), Menghao Jin(金蒙豪), Yungui Ma(马云贵), Bo Liu(刘波), Tiejun Zhou(周铁军)
Chin. Phys. B. 34, 098501 (2025). DOI: 10.1088/1674-1056/ade42c | CSTR: 32038.14.CPB.ade42c

Fully spin-polarized, valley-polarized and spin-valley-polarized electron beam splitters utilizing zero-line modes in a three-terminal device

Xiao-Long Lü(吕小龙), Jia-En Yang(杨加恩), Hang Xie(谢航)
Chin. Phys. B. 33, 068502 (2024). DOI: 10.1088/1674-1056/ad2609

Interfacial DMI in Fe/Pt thin films grown on different buffer layers

Wen-Jun Zhang(张文君), Fei Wei(魏菲), Bing Liu(刘冰), Yang Zhou(周阳), Shi-Shou Kang(康仕寿), Bing Sun(孙兵)
Chin. Phys. B. 33, 048501 (2024). DOI: 10.1088/1674-1056/ad1b41

Antiferromagnetic ordering and strain effects in monolayer quadrilateral FeS_2

Zhihao Li(李志豪)[1,2,3,†], Junlin Wang(王君林)[5,†], Guanqi Li(李冠祺)[5], Yao Li(黎遥)[1,2], Liang He(何亮)[1,2], Jing Wu[4,5], Yongbing Xu[1,2,3,4,‡], and Xianyang Lu(陆显扬)[1,2,3,§]

[1] *National Key Laboratory of Spintronics, Nanjing University, Suzhou* 215163, *China*
[2] *Jiangsu Provincial Key Laboratory of Advanced Photonic and Electronic Materials, School of Electronic Science and Engineering, Nanjing University, Nanjing* 210093, *China*
[3] *School of Integrated Circuits, Nanjing University, Suzhou* 215163, *China*
[4] *York–Nanjing International Center for Spintronics (YNICS), School of Physics Engineering and Technology, University of York, York YO*10 5*DD, UK*
[5] *School of Integrated Circuits, Guangdong University of Technology, Guangzhou* 510006, *China*

(Received 26 August 2025; revised manuscript received 1 November 2025; accepted manuscript online 6 November 2025)

Two-dimensional (2D) transition metal dichalcogenides have garnered growing attention for spintronics devices due to their special atomic structure and rich physical properties. Here, we report a monolayer quadrilateral FeS_2 material with antiferromagnetic (AFM) ordering identified by particle swarm optimization (PSO) global structure search. Using first-principles calculations and micromagnetic simulations, we demonstrate that monolayer quadrilateral FeS_2 is an antiferromagnetic metal with the easy axis of the ground state along the c axis and a high Néel temperature (T_N). We have further found that the magnetic moment of Fe atoms and magnetic states are strongly modulated by the biaxial strain in a range from -8% to 8%. When compressive strains of 2% and 6% are applied, easy axis rotation and T_N increase occur, respectively. These findings establish a foundational framework for the development of FeS_2-based AFM spintronics for potential high-speed device applications.

Keywords: spintronics, 2D materials, FeS_2, first-principles calculations, structure prediction

PACS: 85.75.–d, 75.75.–c, 63.20.dk, 88.10.gc

DOI: 10.1088/1674-1056/ae1c1f **CSTR:** 32038.14.CPB.ae1c1f

1. Introduction

Two-dimensional (2D) transition metal dichalcogenides (TMDCs) have attracted considerable interest for fundamental studies and novel electronic devices, owing to a rich variety of physical properties that span semiconducting,[1,2] metallic,[3] half-metallic,[4,5] semi-metallic,[6,7] and even superconducting[8] systems. Among the TMDC families, iron disulfide (FeS_2), in particular, has been extensively studied due to the natural abundance of its constituent elements, low material cost, and the versatile methods for synthesizing its thin films and various nanostructures. Depending on its atomic structure and growth method, 2D FeS_2 can display an appreciable variety of properties.[9,10]

An immense theoretical effort has been devoted to understanding the various structures of FeS_2. Early computational studies focused on bulk phases such as pyrite and marcasite, investigating their optical properties, band structures, and mechanical stability under pressure.[11–13] More recent research has explored novel nanostructures with several-atom thicknesses, such as T-FeS_2 and S-FeS_2,[14] as well as the influence of strain on the electronic properties of FeS_2 monolayers.[15] However, despite these substantial theoretical, computational, and experimental efforts, the exploration of a stable FeS_2 magnetic monolayer remains a major challenge.

To address this gap, powerful computational structure prediction methods, such as Crystal structure AnaLYsis by Particle Swarm Optimization (CALYPSO), provide a pathway to discovering novel 2D materials.[16–18] These predictive approaches are especially pertinent to the search for materials tailored for next-generation technologies.[19,20] A particularly promising area is antiferromagnetic (AFM) spintronics, which seeks to leverage the unique advantages of AFM materials, namely their zero net magnetization and ultrafast spin dynamics, for high-speed device applications.[21–24]

In this work, we report the discovery of a novel monolayer FeS_2 crystal structure with AFM ordering, identified using the PSO technique implemented in the CALYPSO package. Through first-principles calculations and micromagnetic simulations, we systematically investigate its magnetic properties and uncover the origin of its high spin state. We demonstrate that this quadrilateral structure possesses excellent stability, as verified by phonon spectra, elastic constants, and for-

[†]These authors contributed equally to this work.
[‡]Corresponding author. E-mail: ybxu@nju.edu.cn
[§]Corresponding author. E-mail: xylu@nju.edu.cn

© 2026 Chinese Physical Society and IOP Publishing Ltd. All rights, including for text and data mining, AI training, and similar technologies, are reserved.

mation energies. Moreover, we show that the electromagnetic properties of this monolayer FeS_2 can be further regulated by biaxial strain, highlighting its potential as a foundational material for developing novel AFM spintronic devices.

2. Computational details

The PSO algorithm is used to find the lowest total energy structure of the FeS_2 monolayer in the CALYPSO package.[25–27] The population size is set at 20, and the number of generations is set to 50 to ensure convergence. Our calculations are all based on density functional theory (DFT) as implemented in the Vienna *Ab initio* Simulation Package (VASP, version 5.4.4).[28,29] The generalized gradient approximation (GGA) method with the Perdew–Burke–Ernzerhof (PBE) functional[30] is used to calculate the electron exchange–correlation energy. Electron–nuclear interactions were described by the projector augmented wave (PAW) method.[31] In reciprocal space, the electronic wave function is extended by the plane wave basis set. The DFT-D3 method[32] is used to calculate the weak van der Waals interactions between adjacent layers. The effective field Coulomb interaction parameter (U_{eff}) is used as 2.0 eV to correct the d strongly correlated electron interaction of Fe atoms, which is taken from Refs. [13,14] and used in the Materials Project for many kinds of compounds containing Fe. A cut-off energy of 520 eV for the plane-wave basis set is adopted. The size of the K grid of the first Brillouin zone is set to $11 \times 11 \times 1$.[33] In the process of structural optimization, all atoms relax until the force on each atom is smaller than 0.01 eV/Å. A vacuum slab of 15 Å is used for separating the cells to mimic the 2D system. The calculation of the phonon dispersion curve is based on the density functional perturbation theory (DFPT)[34] by using the PHONOPY package.

3. Results and discussion

The most stable structure of monolayer FeS_2 is identified after 50 generations of PSO global structure search. Figure 1(a) shows the top and side view of the optimized structure of the FeS_2 monolayer, which crystallizes in the tetragonal space group, $P\bar{4}m2$, with each Fe atom bonding with four S atoms to form tetrahedral coordination. The unit cell of the FeS_2 monolayer contains one Fe and two S atoms with the optimized lattice parameter $a = b = 3.46$ Å. The structure of the FeS_2 monolayer can be viewed as a sandwich structure, in which the Fe atomic layer is sandwiched between the top and bottom S atomic layers. The thickness of the FeS_2 monolayer is 2.57 Å, and the bond length of Fe–S is 2.16 Å. The distances between the nearest and the next-nearest neighbor Fe atoms are 3.46 Å and 4.90 Å, respectively.

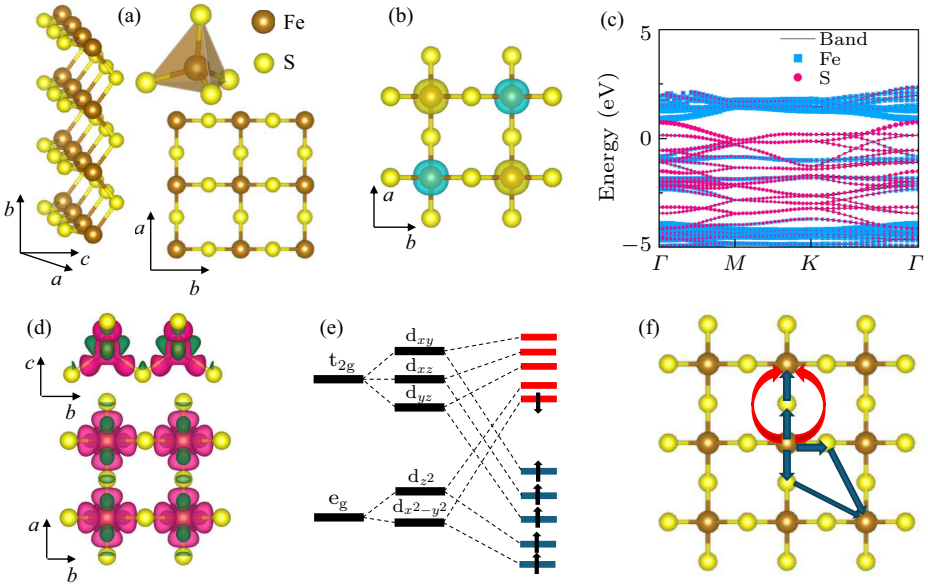


Fig. 1. (a) Atomic structures of monolayer quadrilateral FeS_2: side view, top view, and tetrahedral coordination. (b) Spin charge distributions of monolayer quadrilateral FeS_2 with an isosurface of 0.048 $e/Å^3$. The contour profile with yellow (blue) indicates a net spin-up (spin-down) polarization. (c) Atom-resolved band structure of monolayer quadrilateral FeS_2 ground state. The Fermi level is set to zero. (d) Side view and top view of differential charge density (isovalue: 0.009 $e/Å^3$). The dark pink and green colors correspond to charge accumulation and depletion, respectively. (e) Splitting of d orbitals of the Fe atom under the quadrilateral crystal field of the FeS_2 monolayer. (f) Schematic diagram of the exchange path between the nearest and the next-nearest neighbor Fe atoms. The blue (red) arrows represent direct exchange (superexchange) interactions.

To study the magnetic properties of single-layer FeS_2, we consider three kinds of magnetic configurations by calculating the energy difference between each configuration to confirm the ground state, as shown in Fig. S1 and Table S1 in supporting materials. The result shows that the total energy of antiferromagnetic (AFM2) ordering is the lowest, indicating that the ground state of the single-layer FeS_2 is antiferromagnetic. The nonmagnetic (NM) state exhibits the highest en-

ergy, showing the importance of considering spin polarization in the calculations. In addition, the same results are obtained for the energy difference under other values of U taken. The spin charge density in the ground state is shown in Fig. 1(b). There is a sizeable magnetic moment of 2.80 μ_B per Fe atom, with the spin density mainly localized on the Fe atoms. In addition, the magnetic moments of each Fe atom in the ground state under different U are shown in Table S1. However, the spin directions of each Fe atom are opposite to each other, resulting in the magnetic moment of the unit cell canceling each other out.

The quadrilateral structure of the FeS_2 monolayer leads to the orbitally resolved band structure shown in Fig. 1(c). The single-layer FeS_2 is metallic. Furthermore, the band structures of monolayer quadrilateral FeS_2 for different U values are shown in Fig. S2. The orbitals near the Fermi energy level are mainly contributed by the p orbitals of S atoms. Most previous studies on single-layer FeS_2 also exhibit metallicity, as shown in Table 1. We also use the Heyd–Scuseria–Ernzerhof (HSE06) hybrid functional[39] to confirm that the ground state and band structure of the monolayer quadrilateral FeS_2 is AFM metallic with 3.61 μ_B per Fe atom, as shown in Fig. S3. This kind of AFM metal film is expected to be applied to AFM-based high-speed spintronic devices.[40]

Table 1. The space group, in-plane lattice constants a and b, magnetism, band gaps E_g, and localized magnetic moments for each Fe (M_{Fe}) of single-layer FeS_2 with different crystal structures obtained by theoretical calculations and experiments. The unit 1 bar = 10^5 Pa.

System	Space group	a (Å)	d_{Fe-S} (Å)	Magnetic	E_g (eV)	M_{Fe} (μ_B)
Quadrilateral FeS_2	$P\bar{4}m2$	3.46	2.16	AFM	Metal	2.80
S-FeS_2[14]	$P21/c$	5.51	2.18	AFM	Metal	
T-FeS_2[14]	$P\bar{3}m1$	3.19	2.28	FM	Metal	2
H-FeS_2[35]	$P63/mmc$	3.15	2.28	FM	Metal	1.67
H-FeS_2[35] (13.7 kbar–59 kbar)	$P63/mmc$	3.02–2.80	2.28–2.26	FM	Half-metal	2.0
H-FeS_2[36]	$P63/mmc$	3.10	2.25	FM	Half-metal	1.42
T-FeS_2[37]	$P\bar{3}m1$	/	2.27	FM	Metal	1.8 (total)
FeS_2(100) monolayer[38]	$P21/c$	5.52	2.14	FM	0.73	/

The origin of high-spin states with a large magnetic moment per Fe atom can be well explained by the influence of the tetrahedral crystal field on the d orbitals of Fe atoms. According to the atomic formal charge, each S atom should gain one electron from the Fe atom ([Ar]$3d^6 4s^2$). This trend of charge transfer from Fe to S atoms can be qualitatively seen in the differential charge density in Fig. 1(d). As schematically illustrated in Fig. 1(e), due to the symmetry of the tetrahedral crystal field, five degenerate d orbitals of the Fe atoms are split into t_{2g} levels (d_{xy}, d_{xz}, and d_{zy}) with higher energy and e_g levels ($d_{x^2-y^2}$ and d_{z^2}) with lower energy under the current axis definition. In the monolayer FeS_2 structure, the tetrahedral crystal field leads to further splitting of the t_{2g} and e_g levels. Consequently, the five d orbitals are no longer degenerate. Following Hund's rule, the six low-lying orbitals are singly occupied by the remaining pair of valence electrons and four unpaired valence electrons on the Fe ion, resulting in a high spin moment. This picture is further supported by the partial DOS (PDOS) of the FeS_2 monolayer in Fig. 2.

For the mechanism of AFM coupling of the FeS_2 monolayer, we further studied the exchange coupling interactions between Fe atoms. The exchange interactions in the system are mainly caused by the direct exchange coupling between Fe atoms and the superexchange mediated by S atoms. The distances between the nearest and the next-nearest neighbor Fe atoms and the possible exchange interaction paths are shown in Fig. 1(f). The distances between the nearest and the next-nearest neighbor Fe–Fe are $d_1 = 3.46$ Å and $d_2 = 4.90$ Å. The direct exchange interactions originate from the direct electronic transitions between the nearest neighbor Fe atoms. At this time, because the 3d orbitals of Fe atoms are partly occupied, the direct exchange interactions are likely to be antiferromagnetic.[41] The superexchange interactions in single-layer FeS_2 follow the Goodenough–Kanamori–Anderson (GKA) rules,[42] which state that the type of magnetic ordering is due to the superexchange interactions between two metal ions bridged by a nonmetal ion mainly depending on the metal–nonmetal–metal bond angle. The angle of Fe–S–Fe is 106.34°, suggesting that the superexchange ordering is weakly antiferromagnetic.

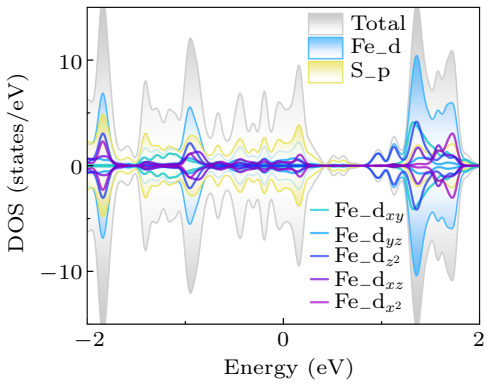


Fig. 2. Total (gray), atom-projected (blue for d orbital of Fe atoms, yellow for p orbital of S atoms), and d orbital evolved density of states on the Fe atom for the FeS_2 monolayer. The Fermi level is set to zero.

Here, the Hamiltonian of the classical Heisenberg model

is used to calculate the exchange coupling constants of Fe[43]

$$H = \sum_{\langle ij \rangle} J_1 \boldsymbol{S}_i \cdot \boldsymbol{S}_j + \sum_{\langle\langle ij \rangle\rangle} J_2 \boldsymbol{S}_i \cdot \boldsymbol{S}_j, \tag{1}$$

where J_1 and J_2 are the nearest and next-nearest neighbor exchange coupling constants, respectively. $\boldsymbol{S}_i$ and $\boldsymbol{S}_j$ are the spin parameters of the transition metal atoms at positions i and j, respectively. According to the configurations of spin directions of the transition metal in different spin states, as shown in Fig. S1, Eq. (1) is simplified as

$$E_{\mathrm{FM}} = E_0 - (4J_1 + 4J_2)S^2, \tag{2}$$

$$E_{\mathrm{AFM1}} = E_0 - (-4J_2)S^2, \tag{3}$$

$$E_{\mathrm{AFM2}} = E_0 - (-4J_1 + 4J_2)S^2. \tag{4}$$

According to the spin quantum number of Fe^{2+}, $S = 2$ is selected. The calculated nearest and next-nearest neighbor exchange coupling constants J_1 and J_2 are -11.85 meV and -1.06 meV, respectively. This indicates that the nearest and next-nearest neighbor exchange interactions are both antiferromagnetic.

To identify the easy axis of monolayer quadrilateral FeS_2, the magnetic anisotropic energy (MAE) with the torque method is computed as implemented in VASP.[44] The calculated MAE = 228.44 μ eV/f.u. shows that the easy axis is along the c-axis out of the plane. We then calculate the Néel temperature (T_N) via the mean field approximations (MFA) written as[45]

$$k_B T_N = \frac{2qJS^2}{3}, \tag{5}$$

where k_B is the Boltzmann constant and q is the number of nearest neighbors of the unit cell. The calculated T_N is 219.80 K, which is higher than the 2D magnets that have been verified. (*e.g.*, the Curie temperatures of $Cr_2Ge_2Te_6$ and CrI_3 are approximately 64 K and 45 K, respectively[46,47]).

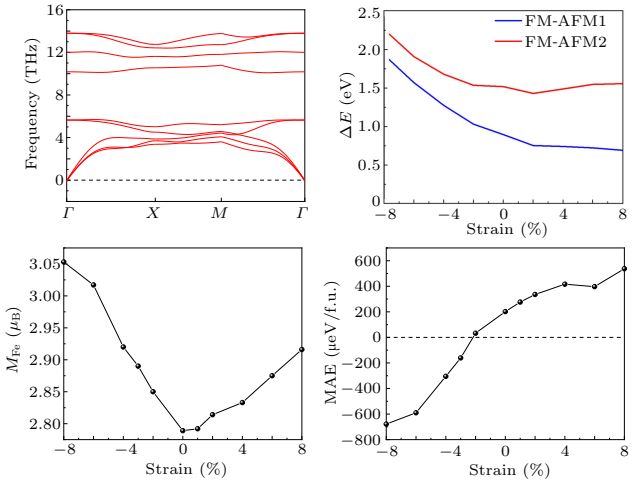


Fig. 3. (a) Phonon dispersion of monolayer quadrilateral FeS_2 using a supercell. (b)–(d) Energy differences between the FM and AFM states (b), the magnetic moment of each Fe atom (c), and ΔMAE (d) of monolayer quadrilateral FeS_2 under biaxial strains ranging from −8% to 8%.

To confirm the dynamic stability of the ground state of the monolayer quadrilateral FeS_2 structure, we calculate its phonon spectrum with the force information obtained from VASP calculations for $3 \times 3 \times 1$ supercells followed by post-processing calculations via the Phonopy package, as shown in Fig. 3(a). Furthermore, the phonon dispersion of monolayer quadrilateral FeS_2 using K-points of $11 \times 11 \times 1$, $13 \times 13 \times 1$, and $15 \times 15 \times 1$ is shown in Fig. S4. Although there are some negligibly small imaginary frequencies near the Γ point due to translational invariance (*i.e.*, the acoustic sum rule), the absence of imaginary modes in the other q points throughout the Brillouin zone shows dynamic stability.[48]

To verify the mechanical and thermodynamic stability of monolayer quadrilateral FeS_2, the stiffness tensor and enthalpy of formation of single-layer FeS_2 were calculated.[49] As shown in Table 2, the stiffness tensor satisfying the Born stability criteria[50] indicates that the material is in a mechanically stable state. The enthalpy of formation is much smaller than zero, proving the thermodynamic stability of the monolayer FeS_2. To further demonstrate the thermodynamic stability, ab initio molecular dynamics (AIMD) simulations of monolayer quadrilateral FeS_2 are shown in Fig. S5.

Table 2. The stiffness tensor (C_{11}, C_{12}, C_{22}, and C_{66}) and enthalpy of formation of monolayer quadrilateral FeS_2.

System	C_{11} (N/m)	C_{12} (N/m)	C_{22} (N/m)	C_{66} (N/m)	E_{form} (eV)
FeS_2	32.06	20.24	32.06	3.61	–24.26

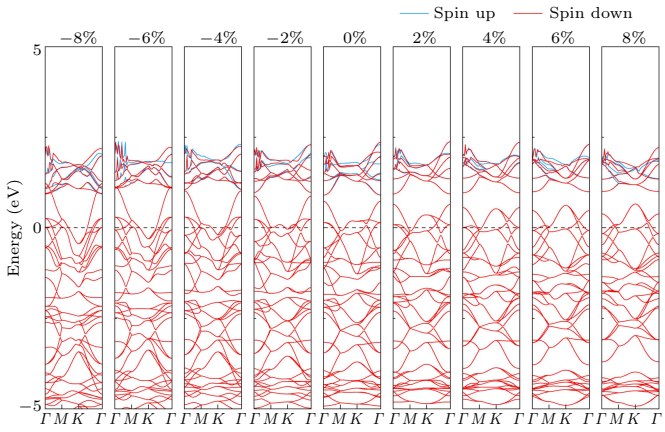


Fig. 4. Band structures of monolayer quadrilateral FeS_2 under biaxial strains ranging from −8% to 8%.

Strain engineering has been widely used to modulate the structural and electromagnetic properties of monolayer TMDC, such as thermal expansion,[51–53] elongated substrate,[54] and mechanical stretching/bending.[55–60] We apply in-plane biaxial strains to monolayer quadrilateral FeS_2. Figure 3(b) shows the energy differences of monolayer quadrilateral FeS_2 with FM and AFM orderings under biaxial strains ranging from −8% to 8%. We observed that the energy difference remains positive in the range of applied biaxial strains, showing that the AFM ground state is unaffected by

the strains. The magnetic moment of Fe atoms gradually increases with increasing strain, as shown in Fig. 3(c). In addition, the MAE and the band structure of monolayer quadrilateral FeS_2 are significantly affected by the biaxial strain. When a tensile strain applied to the material increases gradually from zero strain, the MAE gradually increases. However, when a compressive strain of 2% is applied, the easy axis of the single-layer FeS_2 flips from out-of-plane to in-plane, as shown in Fig. 3(d). As shown in Fig. 4, the trend of the change in the band structure with biaxial strain shows that monolayer quadrilateral FeS_2 remains metallic within the applied strain range.

In addition, we calculated the temperature-dependent magnetization of FeS_2. The calculation of the T_N of FeS_2 is provided by Vampire 5.0.[61] The energy of the system is described by the following Hamiltonian, which includes all the energy contributions to the magnetic behavior of the system, as well as the Heisenberg form of exchange:

$$H = -\sum_{i<j} J_{ij}\boldsymbol{S}_i \cdot \boldsymbol{S}_j - \sum_i k_u^i (\boldsymbol{S}_i \cdot \hat{e}) - \mu_0 \sum_i \mu_S^i \boldsymbol{S}_i \cdot \boldsymbol{H}_{app} + H_{demag}, \quad (6)$$

where k_u^i is the uniaxial anisotropy energy on site i along the axis $\hat{e}$, μ_0 is the permeability constant, μ_S^i is the atomic spin moment, $\boldsymbol{H}_{app}$ is the Hamiltonian of externally applied magnetic fields, and H_{demag} is the Hamiltonian of demagnetization fields. The parameters in the simulation are obtained by ab initio density functional theory (DFT) calculations, including nearest-neighbor exchange interactions and next-nearest-neighbor exchange interactions. The crystal structure of the model is based on the structure used in the VASP calculations with a lattice constant of 3.46 Å and a system size of 50 nm×50 nm. We incorporate the thermal effect into the model by introducing the stochastic field into the effective field in the atomistic Landau–Lifshitz–Gilbert equation. Within this approach, the stochastic field is introduced as a white noise term, whose properties are in agreement with the fluctuation–dissipation theorem and correctly lead to the Boltzmann equilibrium distribution.[62,63] The mean magnetization of the FeS_2 sublattice and exchange strength are given in Fig. 5.

In Fig. 5(a), when the biaxial strain is larger than 4%, J_2 is in the ferromagnetic phase. According to the results in Fig. 5(b), the T_N of the sublattice is near 80 K. As illustrated in Fig. 5(c), the peak positions of the magnetic susceptibility under various strains are in excellent agreement with the transition temperatures identified from the mean magnetization curves, which robustly confirms the antiferromagnetic phase transition. It should be noted that the T_N calculated using the MFA is a known overestimation.[64] This is because the MFA model overstates the stability of the magnetic order by neglecting crucial thermal spin fluctuations. The physical origin of this discrepancy is that the MFA model replaces dynamic spin interactions with a static average field, thereby neglecting the crucial thermal spin fluctuations that act to destabilize the magnetic order. Under the application of 6% biaxial compressive strain, the huge antiferromagnetic exchange coupling increases T_N to 100 K. This strain tunability can be attributed to changes in lattice deformation and interactions between electron clouds of atoms under strain, thus providing us with the opportunity to tune the band structure and magnetic properties of 2D TMDC.[65]

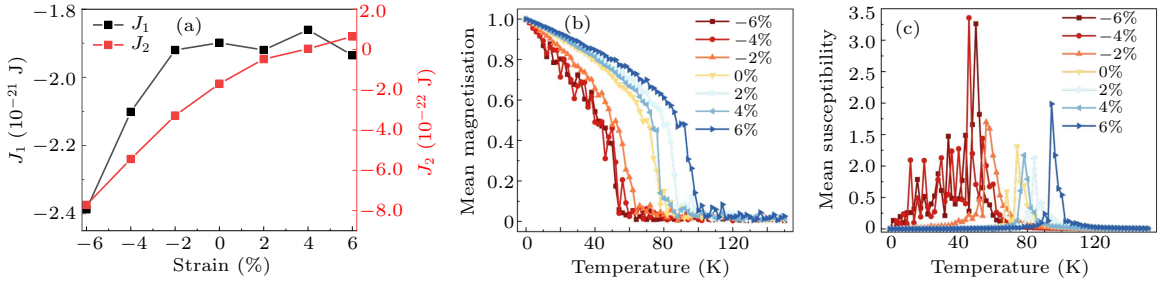


Fig. 5. (a) The biaxial strains-dependent nearest exchange strength J_1 and next nearest exchange strength J_2. The mean magnetization (b) and the magnetic susceptibility (c) of the FeS_2 sublattice under biaxial strains.

4. Conclusion

In summary, we predict a monolayer quadrilateral metal FeS_2 with AFM via PSO global structure search and first-principles calculation. This quadrilateral structure has sufficient kinetic, mechanical, and thermodynamic stability. The Fe atoms of the single-layer FeS_2 are in a high-spin state with 3.6 μ_B. The single-layer quadrilateral FeS_2 exhibits a sizable MAE with the in-plane easy axis. We further estimate that T_N is 80 K using micromagnetic simulations, which means that it has the potential to be used in spintronics devices. At biaxial strains of −8% to 8%, FeS_2 maintains an AFM ground state and a larger magnetic moment. The rotation of the easy axis and the increase in T_N occurred when −2% and −6% strain was applied, respectively. The remarkable electromagnetic properties of monolayer quadrilateral FeS_2, such as the magnetic moment, band structure and T_N tunable by biaxial strain, make it a candidate 2D material for high-speed spintronic nanodevices.

Data availability

The data that support this work are available in the article and supplementary information file. Further raw data are available from the corresponding author upon request.

Acknowledgements

Project supported by the National Key Research and Development Program of China (Grant Nos. 2024YFA1408801, 2024YFA1408803, and 2021YFB3601600), the National Natural Science Foundation of China (Grant Nos. 12241403, 12474117, 62427901, and 12304136), Guangdong Basic and Applied Basic Research Foundation (Grant Nos. 2022A1515110863 and 2023A1515010837), the Science and Technology Project of Guangdong Province, (Grant No. 2023QN10X275), and the Project for Maiden Voyage of Guangzhou Basic and Applied Basic Research Scheme (Grant No. 2024A04J4186).

References

[1] Liu L, Li T and Gong X, *et al.* 2025 *Nat. Mater.* **24** 1195
[2] Jiang H, Zhang X, Chen K, He X, Liu Y, Yu H, Gao L, Hong M, Wang Y, Zhang Z and Zhang Y 2025 *Nat. Mater.* **24** 188
[3] Watson M D, Date M, Louat A and Schröter N B 2024 *Phys. Rev. B* **110** L121121
[4] Vikraman D, Hussain S, Karuppasamy K, Sanmugam A, Kathalingam A, Manikandan R, Jung J, Alfantazi A and Kim H S 2025 *Int. J. Energy Res.* **2025** 5553294
[5] Liang J, Sun J, Cao X, Li X, Chen X, Xing R and Kong J 2025 *Adv. Sci.* **12** 2502241
[6] Im C Y, Lee G Y, Kim J G, Choi J H and Kim S J 2025 *Adv. Mater.* **37** 2501261
[7] Feng R, Zhang Y, Li J, Li Q, Bao C, Zhang H, Chen W, Tang X, Yaegashi K, Sugawara K, Sato T, Duan W, Yu P and Zhou S 2025 *Nat. Commun.* **16** 2667
[8] Ye J, Zhang Y J, Akashi R, Bahramy M S, Arita R and Iwasa Y 2012 *Science* **338** 1193
[9] Qin H, Jia J, Lin L, Ni H, Wang M and Meng L 2018 *Mater. Sci. Eng. B* **236** 104
[10] Kaur G, Kaur M, Thakur A and Kumar A 2019 *J. Cluster Sci.* **31** 899
[11] Bullett D 1982 *J. Phys. C Solid State Phys.* **15** 6163
[12] Liu S, Li Y, Yang J, Tian H, Zhu B and Shi Y 2013 *Phys. Chem. Miner.* **41** 189
[13] Wen X, Liang Y, Bai P, Luo B, Fang T, Yue L, An T, Song W and Zheng S 2017 *Physica B* **525** 119
[14] Zhang H, Dai Y M and Liu L M 2015 *Comput. Mater. Sci.* **101** 255
[15] Xiao P, Fan X L, Liu L M and Lau W M 2014 *Phys. Chem. Chem. Phys.* **16** 24466
[16] Zhang J, Sun E, Feng X, Liu H, Redfern S A T, Kanchana V, Liu G and Wang H 2018 *Phys. Chem. Chem. Phys.* **20** 29472
[17] Wang X, Liu Y, Chen X, Zhang P and Liu X 2020 *Phys. Chem. Chem. Phys.* **22** 8827
[18] Hu K, Chen Q J and Xie S Y 2020 *J. Phys. Condens. Matter* **32** 085402
[19] Jin W, Zhang G, Wu H, Yang L, Zhang W and Chang H 2023 *Chin. Phys. Lett.* **40** 057301
[20] Liu Y S, Sun H, Hu C S, Wu Y J and Zhang C W 2023 *Chin. Phys. B* **32** 027101
[21] Guo Z, Wang X, Wang W, Zhang G, Zhou X and Cheng Z 2025 *Adv. Mater.* **37** 2505779
[22] Song C, Zhang R, Liao L, Zhou Y, Zhou X, Chen R, You Y, Chen X and Pan F 2021 *Prog. Mater. Sci.* **118** 100761
[23] Manchon A, Železný J, Miron I M, Jungwirth T, Sinova J, Thiaville A, Garello K and Gambardella P 2019 *Rev. Mod. Phys.* **91** 035004
[24] Li Q, Zhen W, Wang N, Shi M, Yu Y, Pan S, Deng L, Cai J, Wang K, Zou L, Zeng Z, Wang Z and Zhang J 2024 *Chin. Phys. Lett.* **41** 107503
[25] Wang Y, Lv J, Zhu L and Ma Y 2012 *Comput. Phys. Commun.* **183** 2063
[26] Wang Y, Lv J, Zhu L and Ma Y 2010 *Phys. Rev. B* **82** 094116
[27] Gao B, Gao P, Lu S, Lv J, Wang Y and Ma Y 2019 *Sci. Bull.* **64** 301
[28] Kresse G and Furthmüller J 1996 *Comput. Mater. Sci.* **6** 15
[29] Cristol S, Paul J, Payen E, Bougeard D, Clémendot S and Hutschka F 2000 *J. Phys. Chem. B* **104** 11220
[30] Perdew J P, Burke K and Ernzerhof M 1996 *Phys. Rev. Lett.* **77** 3865
[31] Blochl P E 1994 *Phys. Rev. B* **50** 17953
[32] Grimme S 2006 *J. Comput. Chem.* **27** 1787
[33] Monkhorst H J and Pack J D 1976 *Phys. Rev. B* **13** 5188
[34] Gonze X and Lee C 1997 *Phys. Rev. B* **55** 10355
[35] Gökoğlu G and Aktürk E 2017 *Mater. Res. Express* **4** 116305
[36] Lan M, Xiang G, Nie Y, Yang D and Zhang X 2016 *RSC Adv.* **6** 31758
[37] Antipina L Y, Kvashnin A G, Sorokin P B and Chernozatonskii L A 2016 *Phys. Chem. Chem. Phys.* **18** 26956
[38] Yakovkin I N and Petrova N V 2016 *Appl. Surf. Sci.* **377** 184
[39] Heyd J, Scuseria G E and Ernzerhof M 2003 *J. Chem. Phys.* **118** 8207
[40] Qiu H, Zhou L, Zhang C, Wu J, Tian Y, Cheng S, Mi S, Zhao H, Zhang Q, Wu D, Jin B, Chen J and Wu P 2020 *Nat. Phys.* **17** 388
[41] Ushakov A, Kukusta D, Yaresko A and Khomskii D 2013 *Phys. Rev. B* **87** 014418
[42] Goodenough J B 1955 *Phys. Rev.* **100** 564
[43] Sivadas N, Daniels M W, Swendsen R H, Okamoto S and Xiao D 2015 *Phys. Rev. B* **91** 235425
[44] Wang X, Wu R, Wang D S and Freeman A 1996 *Phys. Rev. B* **54** 61
[45] Halilov S, Eschrig H, Perlov A Y and Oppeneer P 1998 *Phys. Rev. B* **58** 293
[46] Huang B, Clark G, Navarro-Moratalla E, Klein D R, Cheng R, Seyler K L, Zhong D, Schmidgall E, McGuire M A, Cobden D H, Yao W, Xiao D, Jarillo-Herrero P and Xu X 2017 *Nature* **546** 270
[47] Gong C, Li L, Li Z, Ji H, Stern A, Xia Y, Cao T, Bao W, Wang C, Wang Y, Qiu Z, Cava R, Louie S, Xia J and Zhang X 2017 *Nature* **546** 265
[48] Liu L, Kankam I and Zhuang H L 2018 *Phys. Rev. B* **98** 205425
[49] Wang V, Xu N, Liu J C, Tang G and Geng W T 2021 *Comput. Phys. Commun.* **267** 108033
[50] Mouhat F and Coudert F X 2014 *Phys. Rev. B* **90** 224104
[51] Gant P, Huang P, Pérez de Lara D, Guo D, Frisenda R and Castellanos-Gomez A 2019 *Mater. Today* **27** 8
[52] Frisenda R, Drüppel M, Schmidt R, Michaelis de Vasconcellos S, Perez de Lara D, Bratschitsch R, Rohlfing M and Castellanos-Gomez A 2017 *npj 2D Mater. Appl.* **1** 10
[53] Plechinger G, Castellanos-Gomez A, Buscema M, van der Zant H S J, Steele G A, Kuc A, Heine T, Schüller C and Korn T 2015 *2D Mater.* **2** 015006
[54] Zhang Q, Chang Z, Xu G, Wang Z, Zhang Y, Xu Z Q, Chen S, Bao Q, Liu J Z, Mai Y W, Duan W, Fuhrer M S and Zheng C 2016 *Adv. Funct. Mater.* **26** 8707
[55] Pang F, Cao F, Lei L, Meng L, Ye S, Xing S, Guo J, Dong H, Hussain S, Gu S, Xu K, Li Y J, Sugawara Y, Ji W, Xu R and Cheng Z 2021 *J. Phys. Chem. C* **125** 8696
[56] Zhao Q, Wang T, Frisenda R and Castellanos-Gomez A 2020 *Adv. Sci.* **7** 2001645
[57] Nakamura H, Mohammed A, Rosenzweig P, Matsuda K, Nowakowski K, Küster K, Wochner P, Ibrahimkutty S, Wedig U, Hussain H, Rawle J, Nicklin C, Stuhlhofer B, Cristiani G, Logvenov G, Takagi H and Starke U 2020 *Phys. Rev. B* **101** 165103
[58] Li Z, Lv Y, Ren L, Li J, Kong L, Zeng Y, Tao Q, Wu R, Ma H, Zhao B, Wang D, Dang W, Chen K, Liao L, Duan X, Duan X and Liu Y 2020 *Nat. Commun.* **11** 1151
[59] John A P, Thenapparambil A and Thalakulam M 2020 *Nanotechnology* **31** 275703
[60] Son J, Kim K H, Ahn Y H, Lee H W and Lee J 2019 *Phys. Rev. Lett.* **123** 036806
[61] Evans R F, Fan W J, Chureemart P, Ostler T A, Ellis M O and Chantrell R W 2014 *J. Phys. Condens. Matter* **26** 103202
[62] Ellis M O A, Evans R F L, Ostler T A, Barker J, Atxitia U, Chubykalo-Fesenko O and Chantrell R W 2015 *Low Temp. Phys.* **41** 705
[63] Brown W F 1963 *Phys. Rev.* **130** 1677
[64] Torelli D and Olsen T 2018 *2D Mater.* **6** 015028
[65] Chen K, Deng J, Yan Y, Shi Q, Chang T, Ding X, Sun J, Yang S and Liu J Z 2021 *npj Comput. Mater.* **7** 79